Analyst

PAPER

View Article Online
View Journal | View Issue

Cite this: *Analyst*, 2026, **151**, 786

Construction of hollow double shell NiMn PBA nanozymes for sensitive sarcosine detection *via* a cascade strategy

Yiwen Sun,† Ying Xie,*† Zixuan Yuan, Yujiao Mao, Huiru Liu, Yiting Zhu, Jinyu Dong and Xiaojun Chen *

Received 28th November 2025,
Accepted 19th December 2025

DOI: 10.1039/d5an01252j

rsc.li/analyst

As sarcosine (SA) is a significant biomarker for the early development of prostate cancer (PCa), its sensitive detection in urine can serve as an effective non-invasive early warning method. Herein, we developed a novel hollow double shell NiMn PBA (NiMn-PBA-DSNB) with outstanding peroxidase-like activity through a facile cation exchange reaction according to the distinct solubility product constants (K_{sp}) of different Prussian blue analogues (PBAs). Moreover, we innovatively proposed an "enzyme–nanozyme" cascade strategy to realize ultrasensitive SA sensing. This system utilized the enzymatic reaction between SA and sarcosine oxidase (SOX) to generate H_2O_2 *in situ*. In the presence of the generated H_2O_2, the NiMn-PBA-DSNB nanozyme can efficiently catalyze the oxidation of 3,3′,5,5′-tetramethylbenzidine (TMB) to produce blue oxTMB. Consequently, the concentration of SA directly correlated with the absorbance value of oxTMB, providing quantitative detection. Based on this dual-enzyme cascade mechanism, a highly sensitive colorimetric assay was developed for the precise analysis of SA. The assay achieved a wide linear range from 8 to 500 μM, with a low detection limit of 1.75 μM, fully fulfilling the requirements for SA sensing in the urine of PCa patients. The method was also successfully applied to the analysis of real human urine samples, achieving recoveries ranging from 102.15% to 104.35% with relative standard deviations of ≤5.03%, which demonstrates its strong potential for clinical application.

1. Introduction

Recently, prostate cancer (PCa) has become the second most common malignancy in the male genito-urinary system.[1] Since PCa often presents with no obvious symptoms in its early stages while treatment options are limited for advanced cases, efficient early diagnosis is critically important. Sarcosine (SA), also known as *N*-methylglycine, is a non-proteinogenic amino acid that acts as an intermediate in the synthesis and degradation of the amino acid glycine.[2] In 2009, Sreekumar *et al.* first proposed that variations in SA levels in the human body are closely associated with the progression of PCa.[3] In contrast to PCa patients, healthy individuals exhibit negligible or undetectable urinary SA concentrations, making its quantitative detection highly valuable for PCa assessment, particularly in early-stage diagnosis. Nowadays, SA has been confirmed as a significant biomarker for the early development of PCa and can be detected in patient urine.[4–7] Yamkamon *et al.* found that the average concentration of SA in the urine of PCa patients is 12.70 ± 3.29 μM, which is significantly higher than that in healthy humans.[8] This notable difference demonstrates that the level of SA in urine can effectively assess the clinical status of PCa patients.

Currently, the primary methods for SA detection, such as chromatography, electrochemical analysis, and fluorescence spectroscopy, are often limited by high instrument costs, lengthy procedures, and complex sample pretreatment requirements.[9–13] In comparison, colorimetry has distinct practical advantages, including low cost and operational simplicity, making it a highly applicable alternative for rapid screening.[14–18] Recently, nanozymes have gained significant interest due to their characteristics of simple preparation, low cost, high stability, *etc.*[19–21] For instance, Yang *et al.* developed oxidase-induced self-assembled nanoflowers ($Cu_3(PO_4)_2$:Ce@SOX), utilizing a multi-enzyme cascade reaction for the dual-mode detection of SA.[22] Zhao *et al.* prepared an Fe_3O_4@SiO_2@$NiCo_2S_4$ nanocomposite using a deep eutectic solvent-assisted hydrothermal method, which demonstrated high precision and excellent reusability for quantifying SA in human urine.[23] Additionally, Prussian blue analogues (PBAs), known for their high specific surface area and excellent electron transport properties, are widely used in biosensing.[24] In particular, Ni-based PBAs often demonstrate enhanced peroxi-

College of Chemistry and Molecular Engineering, State Key Laboratory of Materials-Oriented Chemical Engineering, Nanjing Tech University, Nanjing, 211816, China. E-mail: xieying@njtech.edu.cn, chenxj@njtech.edu.cn
† These authors contributed equally to this work.

dase (POD)-like activity and have been widely used in colorimetric assays.[25–27] In our previous work, we successfully synthesized Mn-PBA-DSNB@Au nanozymes with high POD-like activity and facilitated the sensitive detection of isoniazid in serum.[28] Furthermore, owing to the differences in solubility product constants among various metal-based PBAs, their enzyme-mimicking activity can be adjusted through cation exchange.[29]

Inspired by previous studies, we successfully synthesized Ni-doped hollow double-shell Prussian blue analogue (NiMn-PBA-DSNB) nanozymes *via* cation exchange (Scheme 1A), which exhibited excellent POD-like activity. Leveraging the specific generation of H_2O_2 during the enzymatic oxidation of SA catalyzed by sarcosine oxidase (SOX), we innovatively constructed a SOX–NiMn-PBA-DSNB "enzyme–nanozyme" cascade catalytic system (Scheme 1B). Based on this dual-enzyme cascade mechanism, we developed a highly sensitive colorimetric assay for precise SA analysis, demonstrating a wide linear range of 8–500 μM with a detection limit of 1.75 μM, fully meeting the requirements for SA detection in clinical samples.

2. Experimental

2.1 Materials and instruments

Manganese acetate ($Mn(CH_3COO)_2{\cdot}4H_2O$) and L-proline (L-Pro) were purchased from Shanghai Macklin Biochemical Co., Ltd. Sodium citrate ($Na_2C_6H_6O_7$), magnesium chloride ($MgCl_2$), calcium chloride ($CaCl_2$), sodium chloride (NaCl), sodium acetate (CH_3COONa), glucose (Glu), glycine (Gly) and hydrogen peroxide (H_2O_2) were purchased from Sinopharm Chemical Reagent Co., Ltd (Shanghai, China). Hydrochloric acid (HCl) and potassium ferricyanide ($K_3[Fe(CN)_6]$) were purchased from Shanghai Lingfeng Chemical Reagent Co., Ltd. Sarcosine oxidase was purchased from J&K Scientific Ltd. 3,3′,5,5′-Tetramethylbenzidine (TMB) was purchased from Sangon Bioengineering Ltd (Shanghai, China). Benzoquinone (PBQ) was purchased from Shanghai Jiuding Chemical Reagent Co., Ltd. Tannins and *o*-phenylenediamine (OPD) were purchased from Sigma Aldrich. Fructose (Fru), maltose (Mal), and L-methionine (L-Met) were purchased from Shanghai Huixing Biochemical Reagent Co., Ltd. Isopropyl alcohol (IPA) was purchased from Shanghai Shenbo Chemical Industry Co., Ltd. Ethylenediaminetetraacetic acid disodium salt (EDTA-2Na) was purchased from Beijing Solarbio Science & Technology Co., Ltd. Nickel chloride ($NiCl_2{\cdot}6H_2O$), L-serine (L-Ser), L-tryptophan (L-Try) and ABTS were provided by Aladdin Biotechnology Co., Ltd.

Scanning electron microscopy (SEM, Quanta FEG 250), transmission electron microscopy (TEM, FEI Talos F200X G2) and powder X-ray diffraction (XRD, MiniFlex600) were used to characterize the surface morphologies and structures of the as-synthesized samples. X-ray photoelectron spectroscopy (XPS, Axis Supra) was used to confirm the surface compositions and chemical states of the samples. A UV-vis spectrophotometer (METASH, UV-5200PC) was used to perform absorbance measurements.

2.2 Synthesis of Mn-PBA-DSNB

Mn-PBA-DSNB was synthesized according to our previous work.[25] Firstly, Mn-PBA was prepared *via* a facile co-precipitation method, which involved mixing solution A (0.6 mmol of $Mn(CH_3COO)_2$ and 1.28 mmol of sodium citrate in 40 mL of H_2O) and solution B (0.4 mmol of $K_3[Fe(CN)_6]$ in 60 mL of H_2O). Then the mixture was aged under continuous stirring at room temperature for 24 h, and the resultant precipitate was collected by centrifugation and drying. The as-synthesized Mn PBA (30 mg) was dispersed in water and reacted with tannic acid (1.5 g) at 85 °C for 6 h. The resulting product was collected, washed, and then treated with 0.24 M HCl for 10 min. Finally, Mn-PBA-DSNB was obtained after another cycle of centrifugation, washing, and drying.

2.3 Synthesis of NiMn-PBA-DSNBs

Utilizing Mn-PBA-DSNB as a precursor, NiMn-PBA-DSNB was synthesized through a cation exchange method. A series of NiMn-PBA-DSNBs were synthesized by adding 10 mg of Mn-PBA-DSNB to 10 mL of an aqueous solution containing different masses (50, 150, 250, and 350 mg) of $NiCl_2{\cdot}6H_2O$. After stirring for 10 min to ensure dispersion, the mixture was reacted at 80 °C for 24 h with stirring. The resulting product was collected by centrifugation, washed with water and ethanol, and dried. The obtained samples were denoted as NiMn-PBA-DSNB(1f), NiMn-PBA-DSNB(3f), NiMn-PBA-DSNB (5f), and NiMn-PBA-DSNB(7f), corresponding to the increasing amount of $NiCl_2{\cdot}6H_2O$ used.

2.4 POD-like activity evaluation of NiMn-PBA-DSNBs

To investigate the effect of the Ni-doping level on the POD-like activity of the PBAs, the catalytic reactions were carried out as follows: preparing a mixture containing 800 μL of NaAc–HAc buffer (0.2 M, pH 4.0), 100 μL of nanozyme (0.2 mg mL^{-1}),

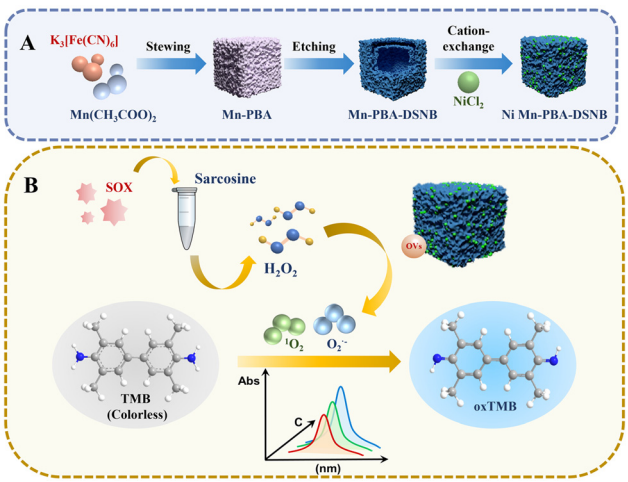

Scheme 1 (A) Schematic diagram of the synthetic process for NiMn-PBA-DSNBs and (B) the colorimetric sensing of sarcosine based on a cascade reaction.

50 μL of TMB (8 mM), and 50 μL of H_2O_2 (10 mM), and incubating it at 37 °C for 10 min. The absorbance from 350 to 800 nm was subsequently measured using a UV-vis spectrophotometer.

A systematic investigation was conducted to identify the optimal reaction conditions for the NiMn-PBA-DSNB(5f) catalyzed TMB/H_2O_2 reaction. The key parameters, including the pH of the HAc–NaAc buffer, reaction time, temperature, and nanozyme concentration, were systematically varied.

2.5 Colorimetric sensing of SA

To ensure the optimal analytical performance, the concentration of the NiMn-PBA-DSNB(5f) nanozyme and the incubation time of SA should be investigated. After determining the optimal conditions, the SA detection process can be divided into the following two steps:

Step 1: 50 μL of SA solution with varying concentrations were incubated with 50 μL of SOX solution (100 U mL^{-1}) at 37 °C for 70 min.

Step 2: to the mixture of step 1, 750 μL of NaAc–HAc buffer (0.2 M, pH 4.0), 100 μL of nanozyme (0.6 mg mL^{-1}), and 50 μL of TMB (8 mM) were added. After reacting at 37 °C for 10 min, the solution was filtered through a 0.22 μm hydrophilic syringe filter, and the absorbance values were measured at wavelengths ranging from 350 to 800 nm using a UV-vis spectrophotometer.

2.6 SA detection in real human urine samples

Urine samples were collected from three healthy volunteers and centrifuged at 10 000 rpm for 10 min, and the resulting supernatant was then filtered through a 0.22 μm aqueous-phase membrane filter. Subsequently, the processed urine was diluted 10-fold with deionized water and mixed with varying concentrations of SA to prepare a series of standard-added samples. Briefly, 50 μL of urine sample, 50 μL of SA solutions at different concentrations, and 50 μL of SOX (100 U mL^{-1}) were mixed and incubated at 37 °C for 70 min. Then, 700 μL of NaAc–HAc buffer, 100 μL of NiMn-PBA-DSNB(5f) nanozyme solution (0.6 mg mL^{-1}), and 50 μL of TMB solution (8 mM) were sequentially added. After reacting at 37 °C for another 10 min, the mixture was filtered and the absorbance was measured.

3. Results and discussion

3.1 Synthesis and structural characterization of NiMn-PBA-DSNBs

As illustrated in Scheme 1A, NiMn-PBA-DSNBs were prepared through a cation exchange reaction using Mn-PBA-DSNBs as the precursor. The Mn-PBA-DSNBs were obtained by etching with tannic acid. As shown in Fig. 1A and Fig. S1, the Mn-PBA-DSNBs were highly uniform and displayed a porous, cubic double-shelled hollow structure.[30] Owing to the higher solubility product (K_{sp}) compared to other PBAs, MnFePBA (K_{sp} = 8.0 × 10^{-13}) undergoes more facile dissociation in aqueous solution, establishing a solid–liquid equilibrium (*e.g.* $Mn_3[Fe(CN)_6]_2 \leftrightarrow 3Mn^{2+} + 2[Fe(CN)_6]^{3-}$).[31] This process releases $[Fe(CN)_6]^{3-}$ ions into the solution, which subsequently react with the introduced Ni^{2+}. As a result, this cation exchange process ultimately yields NiMn-PBA DSNBs with a retained original double-layered structure. Moreover, to investigate the effect of the Ni doping level on the cation exchange process, the amount of the Ni source was varied (50, 150, 250, and 350 mg). The corresponding products obtained were designated as NiMn-PBA-DSNB(1f), NiMn-PBA-DSNB(3f), NiMn-PBA-DSNB(5f), and NiMn-PBA-DSNB(7f). SEM (Fig. S1C) and TEM images (Fig. 1B–E) revealed that the NiMn-PBA-DSNBs retained a well-defined double-shelled structure with a consistent size of approximately 600 nm after the cation exchange reaction. Furthermore, the maintenance of this architecture indicated that the cation exchange process and the amount of Ni salt used had no significant impact on the structure of the nanozyme.[32] Meanwhile, as displayed in Fig. 1F, the EDS mapping of NiMn-PBA-DSNB(5f) distinctly shows the co-existence of Mn, Fe, and Ni elements.

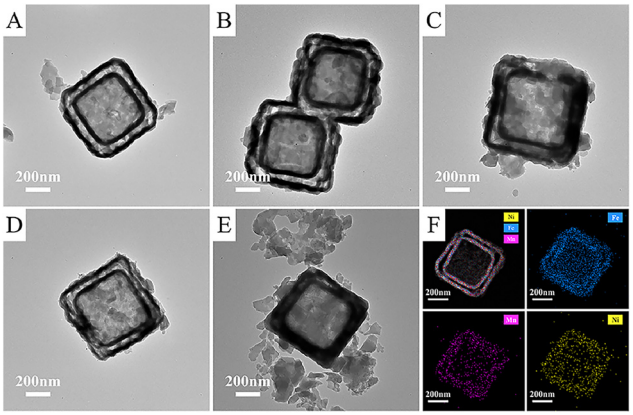

Fig. 1 TEM images of (A) Mn-PBA-DSNB, (B) NiMn-PBA-DSNB(1f), (C) NiMn-PBA DSNB(3f), (D) NiMn-PBA-DSNB(5f), and (E) NiMn-PBA-DSNB (7f); and (F) EDS mapping images of NiMn-PBA-DSNB(5f).

Additionally, XRD characterization (Fig. 2A) showed that a series of resulting NiMn-PBA-DSNB samples and the precursor Mn-PBA-DSNB exhibited similar primary diffraction peaks with Mn-PBA (JCPDS no. 51-1896). Distinct peaks at 2θ values of 17.54°, 24.89°, and 35.51° were assignable to the (200), (220), and (400) crystal planes of the PBA structure, respectively.[30,32] Consequently, our results indicated that the crystal phase of the primary Mn-PBA remains unaffected by either chemical etching or Ni doping. These findings demonstrated the exceptional structural stability of the fabricated nanozymes. Moreover, XPS was employed to analyze the chemical composition and elemental valence states of NiMn-PBA-DSNB(5f). As indicated in Fig. S2, the survey spectrum confirmed the presence of Mn, Fe, Ni, C, N, and O elements. Due to the overlap with the strong $NiL_2M_{23}M_{45}$ Auger peak, accurate fitting of the Mn 2p region was very hard.[33] Nevertheless, as shown in the XPS spectrum in Fig. 2B, the Mn

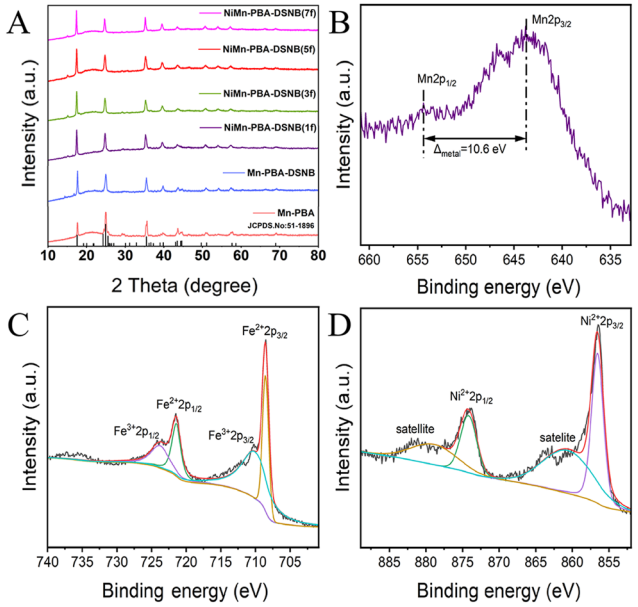

Fig. 2 (A) XRD patterns of Mn PBA, Mn-PBA-DSNB, NiMn-PBA-DSNB (1f), NiMn-PBA-DSNB(3f), NiMn-PBA-DSNB(5f), and NiMn-PBA-DSNB (7f); and XPS spectra of NiMn-PBA-DSNB(5f): narrow scans of (B) Mn 2p, (C) Fe 2p and (D) Ni 2p.

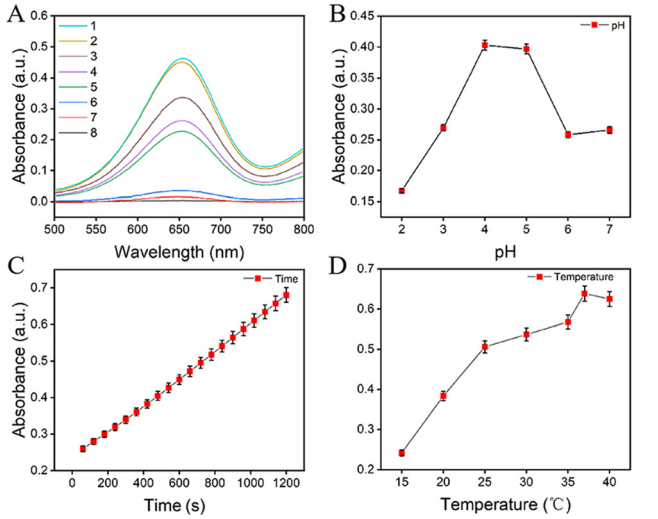

Fig. 3 Optimal reaction conditions: effects of (A) different reaction systems (1: Mn-PBA-DSNB(5f) + H_2O_2 + TMB, 2: NiMn-PBA-DSNB(3f) + H_2O_2 + TMB, 3: NiMn-PBA-DSNB(7f) + H_2O_2 + TMB, 4: NiMn-PBA-DSNB(1f) + H_2O_2 + TMB, 5: Mn-PBA-DSNB + H_2O_2 + TMB, 6: NiMn-PBA-DSNB(5f) + TMB, 7: H_2O_2 + TMB, 8: TMB), (B) pH, (C) time and (D) temperature.

$2p_{3/2}$ and Mn $2p_{1/2}$ peaks were observed at binding energies of 643.8 eV and 654.4 eV, respectively, with a spin-energy separation of 10.6 eV. According to the research by Kosova *et al.*, this observation suggested that the Mn ions in our sample likely exist in mixed valence states of Mn^{4+} and Mn^{3+}. In particular, at low Mn concentrations, the predominant species is expected to be Mn^{3+}.[34,35] Peak fitting of the Fe 2p spectrum (Fig. 2C) clearly revealed characteristic peaks for both Fe^{2+} and Fe^{3+}. The binding energies for Fe^{2+} $2p_{3/2}$ and Fe^{2+} $2p_{1/2}$ were observed at 708.55 eV and 721.43 eV, respectively, while those for Fe^{3+} $2p_{3/2}$ and Fe^{3+} $2p_{1/2}$ were located at 710.08 eV and 723.76 eV.[36,37] Similarly, deconvolution of the Ni 2p spectrum (Fig. 2D) showed two main peaks at 856.57 eV and 874.18 eV, corresponding to Ni^{2+} $2p_{3/2}$ and Ni^{2+} $2p_{1/2}$, respectively. In addition, two distinct satellite peaks were identified at 860.63 eV and 878.92 eV.[38,39] These features confirmed that Ni was incorporated into the nanozyme in the divalent oxidation state (Ni^{2+}).

3.2 POD-like activity of NiMn-PBA-DSNBs

During the investigation of enzyme-like activity, we employed TMB as the chromogenic substrate to evaluate the POD-like activity of a series of NiMn-PBA-DSNB nanozymes with varying Ni doping levels. As depicted in Fig. 3A, the introduction of Ni^{2+} markedly improved the catalytic performance relative to the pristine Mn-PBA-DSNB. The POD-like activity of NiMn-PBA-DSNBs continued to improve with increasing Ni content, reaching a maximum when the doping amount was 250 mg (in the sample designated as NiMn-PBA-DSNB(5f)). This sample achieved the highest absorbance value of 0.46, over twice that of Mn-PBA-DSNB. Therefore, NiMn-PBA-DSNB(5f) with the best enzyme-like activity was selected as the nanozyme for the subsequent colorimetric detection. Furthermore, control experiments were performed under identical reaction conditions. No significant absorption at 652 nm was observed for the following systems: TMB alone, TMB + H_2O_2, and NiMn-PBA-DSNB(5f) + TMB. These results indicated that the interference from TMB autoxidation or the direct reaction between TMB and H_2O_2 is negligible in the POD-like activity assay. In addition, the very weak signal in the NiMn-PBA-DSNB(5f) + TMB system confirmed that the nanozyme exhibited POD-like activity but no significant oxidase-like activity.

Subsequently, reaction conditions for NiMn-PBA-DSNB(5f) were optimized (Fig. 3). The catalytic activity increased in the pH 2.0–4.0 range, remained nearly unchanged at pH 4.0–5.0, and significantly decreased at pH 6.0–7.0, indicating that NiMn-PBA-DSNB(5f) exhibited excellent POD-like activity in weakly acidic environments.[40,41] As shown in Fig. 3D, the enzyme-like activity of NiMn-PBA-DSNB(5f) increased significantly within the temperature range of 15–37 °C and reached its maximum at 37 °C. This optimum coincided with physiological temperature, making it highly relevant for human urine sample analysis. The subsequent decrease in activity at higher temperatures was likely due to the thermal instability of the oxidative intermediate species.[42] Fig. 3C and Fig. S3 show that the POD-like activity of NiMn-PBA-DSNB(5f) rose steadily with increasing time and nanozyme concentration. Balancing the need for a low-cost and rapid colorimetric assay with the demand of high instrumental precision from the UV-vis spectrophotometer, we defined the final optimal reaction conditions as follows: NaAc–HAc buffer (0.2 M, pH 4.0), reaction time of 10 min, reaction temperature of 37 °C and NiMn-PBA-DSNB(5f) at a concentration of 0.02 mg mL^{-1}.

3.3 Steady-state kinetic analysis of NiMn-PBA-DSNB(5f)

To investigate the kinetics of the NiMn-PBA-DSNB nanozyme, varying concentrations of TMB and H_2O_2 were used while keeping the other reaction conditions constant. Specifically, the Michaelis–Menten curve for TMB (Fig. 4A) was generated using different TMB concentrations (0.1–1.0 mM) with a fixed H_2O_2 concentration (0.5 mM). The curve for H_2O_2 (Fig. 4C) was generated using different H_2O_2 concentrations (0.2–1.0 mM) with a fixed TMB concentration (0.4 mM). By recording the characteristic absorbance peak at 652 nm, the Michaelis–Menten constant (K_m) and the maximum reaction rate (V_{max}) for the H_2O_2/TMB/NiMn-PBA-DSNB(5f) reaction system were calculated. The data were then fitted to Lineweaver–Burk double reciprocal plots (Fig. 4B and D). All kinetic parameters were derived from the Michaelis–Menten equation:[43]

$$V_0 = V_{max} \times [S]/(K_m + [S]) \quad (1)$$

In the equation, V_0 denotes the initial velocity and [S] represents the substrate concentration.[44,45] K_m is a key parameter for evaluating the enzyme–substrate affinity, with a lower K_m value indicating higher affinity. Using TMB as the substrate, the K_m value for NiMn-PBA-DSNB(5f) was determined to be 0.53 mM, which is close to that of natural horseradish peroxidase (HRP, 0.43 mM). Notably, the nanozyme's K_m value for H_2O_2 was 0.252 mM, approximately 14.7 times lower than that of HRP (3.7 mM), indicating a significantly stronger affinity for H_2O_2. This result suggested that NiMn-PBA-DSNB(5f) exhibited superior POD-like activity compared to HRP and most reported nanozymes such as Mn-only and Au-modified PBAs (Table S1). As a critical kinetic descriptor, V_{max} enables comparative evaluation of catalytic activities, mechanistic investigations, and rational design of nanozymes.[46] NiMn-PBA-DSNB(5f) achieved values of 5.21×10^{-8} Ms^{-1} (with TMB) and 4.22×10^{-8} Ms^{-1} (with H_2O_2). These values exceed most nanozymes listed in Table S1, underscoring its fast catalytic kinetics.

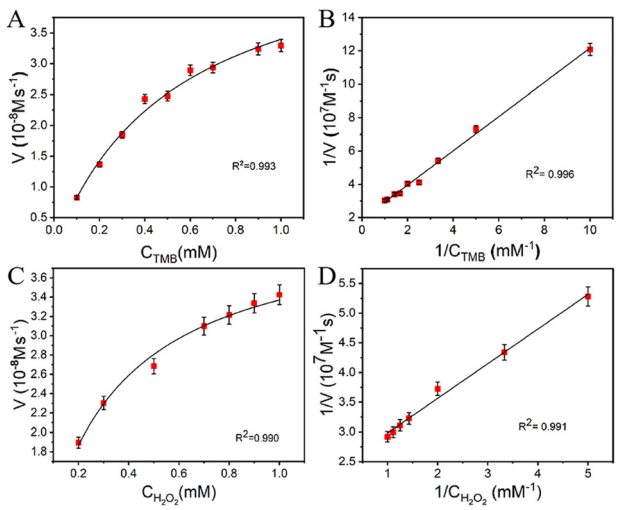

Fig. 4 Michaelis–Menten curves of NiMn-PBA-DSNB(5f) for (A) TMB and (C) H_2O_2. Lineweaver–Burk plots of NiMn-PBA-DSNB(5f) for (B) TMB and (D) H_2O_2.

3.4 Mechanistic study of NiMn-PBA-DSNB(5f)

To further elucidate the catalytic mechanism of the NiMn-PBA-DSNB(5f) nanozyme's POD-like activity, we performed radical trapping experiments using specific scavengers: EDTA-2Na for oxygen vacancies (OVs), PBQ for superoxide anions ($O_2^{\bullet-}$), L-histidine for singlet oxygen ($^1O_2$), and isopropanol (IPA) for hydroxyl radicals ($^{\bullet}OH$). As shown in Fig. 5B, the absorbance at 652 nm significantly decreased with the addition of increasing concentrations of EDTA-2Na, PBQ, and L-histidine. However, no obvious absorbance change was observed in the presence of IPA, even at higher concentrations. Therefore, these experimental results indicate that OVs, $O_2^{\bullet-}$, and $^1O_2$ played key roles in the catalytic process. We proposed that the POD-like activity of the NiMn-PBA-DSNB(5f) nanozyme may proceed through the following mechanism: first, chemical etching alters the metal active sites, inducing crystalline defects on the catalyst surface that lead to the formation of OVs.[47,48] Furthermore, the doping of Ni^{2+} may promote radical generation by regulating the surface adsorption capacity and electron transfer efficiency of the catalyst.[49] Hence, during the reaction, OVs act as electron-rich active sites that strongly adsorb H_2O_2, accelerating the electron transfer between the NiMn-PBA-DSNB and H_2O_2 and leading to the generation of $O_2^{\bullet-}$. In addition, $^1O_2$ is another key active species in the POD-like catalytic process, which was produced *via* the Russell mechanism. In this pathway, the NiMn-PBA-DSNB catalyzes the conversion of H_2O_2 into alkyl peroxy radicals ($ROO^{\bullet}$) as reaction intermediates. Two $ROO^{\bullet}$ radicals combine into a transition-state adduct, which subsequently undergoes structural rearrangement to yield $^1O_2$ together with $O_2^{\bullet-}$.

3.5 Colorimetric detection of SA

For the sensing of SA, we constructed a SOX–NiMn-PBA-DSNB "enzyme–nanozyme" cascade catalytic system. In this system, the H_2O_2 produced by the SOX-catalyzed oxidation of SA is efficiently utilized by the NiMn-PBA-DSNB nanozyme *via* its POD-like activity, leading to signal amplification and conversion. Under the catalysis of SOX, SA can be specifically converted into H_2O_2, which then oxidizes TMB to generate oxTMB in the presence of NiMn-PBA-DSNB(5f). Based on the estab-

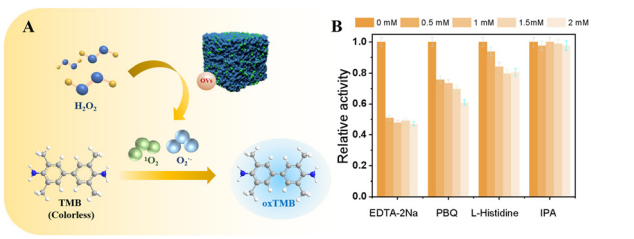

Fig. 5 (A) The proposed reaction mechanism. (B) Effect of different radical trapping agents on the relative activity of the TMB/H_2O_2/NiMn-PBA-DSNB system.

lished linear relationship between SA concentrations and absorbance values, sensitive detection of SA can be achieved.[50] To establish a sensitive detection method for SA, we optimized the concentration of the NiMn-PBA-DSNB(5f) nanozyme and the SA-SOX incubation time, considering that the H_2O_2 yield depends on the initial SA concentration when reacted with constant SOX activity.[51] As shown in Fig. 6A, the absorbance of the reaction system at 652 nm gradually increased with the rising concentration of the NiMn-PBA-DSNB(5f) nanozyme, showing a trend toward saturation at 0.1 mg mL^{-1}. From Fig. 6B, it can be observed that the absorbance value increased with the prolongation of the incubation time between SA and SOX, approaching saturation at 70 min, indicating the completion of the reaction between SA and SOX.[52,53] Considering the cost-effectiveness and time efficiency of colorimetric detection, and in combination with previous optimization results of POD-like activity, the final reaction system was determined as follows: 50 μL of SA at different concentrations was incubated with 50 μL of SOX (100 U mL^{-1}) at 37 °C for 70 min. Subsequently, 750 μL of NaAc–HAc buffer, 100 μL of NiMn-PBA-DSNB(5f) solution (0.6 mg mL^{-1}), and 50 μL of TMB solution (8 mM) were added. The mixture was reacted at 37 °C for another 10 min and filtered through a water-based syringe filter, and then the absorbance was measured. As shown in Fig. 6D, the absorbance value at 652 nm exhibited a linear relationship with SA concentration in the range of 8–500 μM. The linear equation was $y = 0.00165x + 0.26127$ ($R^2 = 0.993$, where y is the absorbance and x is the SA concentration), with a LOD of 1.75 μM ($3\sigma/k$). This demonstrates that our colorimetric sensor is capable of precisely quantifying SA at its cutoff level (25.0 μM) for early PCa diagnosis.[54] Compared with previously reported methods in Table S2, this SA sensor featured a practical wider linear range and a lower LOD.

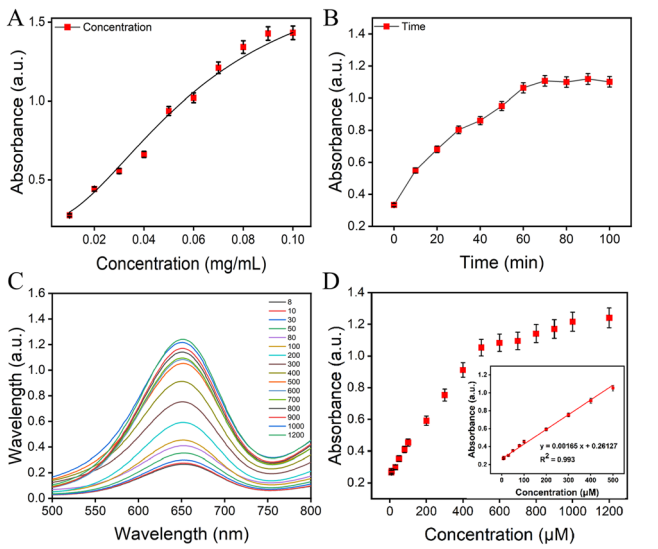

Fig. 6 Optimization of NiMn-PBA-DSNB(5f) concentration (A) and SA–SOX incubation time (B) for SA detection. (C) UV-vis absorption spectra of the SA/SOX/TMB/NiMn PBA-DSNB system at different SA concentrations. (D) Corresponding linear calibration plots for SA detection (the inset shows the standard curve).

3.5 Anti-interference and stability

To evaluate the anti-interference capability of the colorimetric sensor, we investigated the potential effects of common coexisting substances in urine, including ions (Na^+, Mg^{2+}, Ca^{2+}), glucose (Glu), maltose (Malt), fructose (Fru), uric acid (UA), and various amino acids such as glycine (Gly), a product of the SOX-SA reaction, L-tyrosine (L-Tyr), L-tryptophan (L-Try), L-serine (L-Ser), L-methionine (L-Met), L-proline (L-Pro) and L-glutamic acid (L-Glu).[55] Different interferents were added to the reaction system at a final concentration of 5 mM (10-fold that of SA). As shown in Fig. 7A, despite the presence of potential interferents at concentrations 10 times that of SA, the absorbance remained virtually unchanged, indicating the high selectivity of the sensor. This outstanding anti-interference performance ensured its high reliability in practical applications involving complex samples. For the stability evaluation of NiMn-PBA-DSNB(5f), the samples were stored at 4 °C for a total duration of 20 days and the POD-like activity was measured at intervals of 3–4 days. As shown in Fig. 7B, no significant decrease in absorbance was observed over 20 days (RSD = 0.98%), indicating that the catalytic activity was well maintained. This result confirms the excellent stability of the nanozyme and its suitability for prolonged storage without significant loss of function.

3.6 SA sensing in real urine samples

To assess the detection accuracy in real samples, the analytical performance of the colorimetric sensor was investigated using human urine samples *via* the standard addition method. Considering the compositional variability among individual urine samples, urine samples from three healthy volunteers (without SA added) were pre-tested. The results showed that the absorbance values of the different urine samples were essentially consistent with those of the standard blank group, indicating that inter-individual differences do not influence the accuracy of our method. Afterwards, we measured the urine samples with different concentrations of SA (20, 125 and 450 μM) and calculated the spiked recovery rates. Each concentration was analyzed in triplicate, and the results are expressed as the mean of these measurements. As summarized in Table 1, the developed SA sensor exhibited recovery rates ranging from 102.15% to 104.35%, with RSDs of 1.21%,

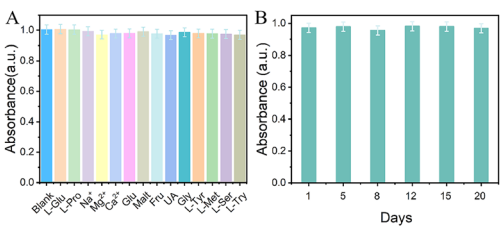

Fig. 7 (A) Absorbance changes at 652 nm after the addition of other interferents. (B) Stability experiments of NiMn-PBA-DSNB(5f).

Table 1 Experimental results on the detection of SA in human urine samples

Sample	Addition amount/μM	Detection amount/μM	Recovery rate (%)	RSD (%, n = 3)
Human urine	20	20.87	104.35	5.03
	125	127.69	102.15	2.07
	450	459.80	102.18	1.21

2.07%, and 5.03%, respectively. These results demonstrated that the colorimetric sensor can meet the requirement for high-precision SA detection in human urine, indicating its potential for early screening and diagnosis of PCa.

4. Conclusion

This study successfully prepared a NiMn-PBA-DSNB nanozyme using a simple synthetic, etching, and cation exchange route. The introduction of Ni significantly enhanced the POD-like activity of the nanozyme. Building on this enhancement and the specific enzymatic reaction of SOX with SA, we constructed a sensitive colorimetric sensor for detecting SA through an enzyme–nanozyme cascade strategy. The developed SA sensor exhibited strong anti-interference capability and excellent stability, with a wide linear detection range of 8–500 μM and a low LOD of 1.75 μM. Furthermore, the sensor was successfully applied to detect SA in human urine samples, achieving satisfactory recovery rates of 102.15%–104.35% and RSDs of ≤5.03%, showing great promise for early PCa diagnosis.

Author contributions

Yiwen Sun: investigation, data acquisition, and writing the original draft. Ying Xie: investigation, data acquisition, funding acquisition, supervision, and writing – review & editing. Zixuan Yuan: resources, formal analysis, and data acquisition. Yujiao Mao: data acquisition and validation. Huiru Liu: formal analysis and validation. Yiting Zhu: formal analysis and validation. Jinyu Dong: validation. Xiaojun Chen: funding acquisition, project administration, supervision, and writing – review & editing. All authors have given approval to the final version of the manuscript.

Conflicts of interest

There are no conflicts to declare.

Data availability

All relevant data are within the manuscript and its supplementary information (SI). Supplementary information: additional figures and tables. See DOI: https://doi.org/10.1039/d5an01252j.

Acknowledgements

This work was financially supported by the National Natural Science Foundation of China (No. 22408159) and the Natural Science Foundation of Jiangsu Province (No. BK20210549).

References

1 F. Crocetto, G. Russo, E. D. Zazzo, P. Pisapia, B. F. Mirto, A. Palmieri, F. Pepe, C. Bellevicine, A. Russo, E. Civita, D. Terracciano, U. Malapelle, G. Troncone and B. Barone, *Cancers*, 2022, **14**, 3272.
2 V. Iyer, R. Rajendran and S. Selvaraj, *Curr. Anal. Chem.*, 2024, **20**, 2–13.
3 A. Sreekumar, L. Poisson, T. Rajendiran and A. Khan, *Nature*, 2009, **457**, 910–914.
4 H. Issaq and T. Veenstra, *J. Sep. Sci.*, 2011, **34**, 3619–3621.
5 M. Miyake and C. Rosser, *Biomarkers Med.*, 2012, **6**, 513–514.
6 B. Cavaliere, B. Macchione, M. Monteleone, A. Naccarato, G. Sindona and A. Tagarelli, *Anal. Bioanal. Chem.*, 2011, **400**, 2903–2912.
7 S. Li, K. Ge, X. Huo, K. Yang, X. Wang and Y. Yang, *J. Colloid Interface Sci.*, 2025, **679**, 401–411.
8 V. Yamkamon, B. Phakdee, S. Yainoy, T. Suksrichawalit, T. Tatanandana, P. Sangkum and W. Eiamphungporn, *EXCLI J.*, 2018, **17**, 467–478.
9 T. Meyer, S. Fox, H. Issaq, X. Xu, L. Chu, T. Veenstra and A. Hsing, *Anal. Chem.*, 2011, **83**, 5735–5740.
10 F. Hamdi, M. Roushani and S. J. Hoseini, *Microchem. J.*, 2025, **208**, 112429.
11 C. Hong, L. Guan, L. Huang, X. Hong and Z. Huang, *New J. Chem.*, 2021, **45**, 10459–10465.
12 Q. Liu, S. Cao, Q. Sun, C. Xing, W. Gao, X. Lu, X. Li, G. Yang, S. Yu and Y. Chen, *J. Hazard. Mater.*, 2022, **436**, 129321.
13 L. Wang, S. Zheng, Z. Cai, F. Wang and C. Li, *Sens. Actuators, B*, 2023, **394**, 134461.
14 J. Du, L. Jiang, Q. Shao, X. Liu, R. Marks, J. Ma and X. Chen, *Small*, 2013, **9**, 1467–1481.
15 A. Tripath and M. P. Styczynski, *Analyst*, 2025, **150**, 1248–1260.
16 N. Passornraprasit, J. Hinestroza, N. Rodthongkum and P. Potiyaraj, *Carbohydr. Polym.*, 2025, **352**, 123134.
17 Y. Wu, C. Ke, Z. Song, H. Zhu, H. Guo, H. Sun and M. Liu, *Analyst*, 2024, **149**, 935–946.
18 G. Chen, H. Shu, L. Wang, K. Bashir, Q. Wang, X. Cui, X. Li, Z. Luo, C. Chang and Q. Fu, *Analyst*, 2020, **145**, 268–276.
19 H. Kwon, D. Kim, K. Seo, Y. Kim, S. Han, T. Kang, M. Soh and T. Hyeon, *Angew. Chem., Int. Ed.*, 2018, **57**, 9408–9412.
20 C. Loynachan, M. Thomas, E. Gray, D. Richards, J. Kim, B. Miller, J. Brookes, S. Agarwal, V. Chudasama, R. McKendry and M. Stevens, *ACS Nano*, 2018, **12**, 279–288.
21 Y. Sun, Y. Zhang, H. Zhang, M. Liu and Y. Liu, *Anal. Chem.*, 2020, **92**, 10668–10676.

22 P. Liu, Q. Sun, Z. Gai, F. Yang and Y. Yang, *Anal. Chim. Acta*, 2024, **1306**, 342586.
23 X. Wang, M. Chen and L. Zhao, *Chem. Eng. J.*, 2023, **468**, 143612.
24 R. Ojha, S. Pal and R. Prakash, *Microchem. J.*, 2021, **171**, 106854.
25 D. Lu, X. Tian, Z. Fu, S. Yang, Y. Qiu, Y. Yang, B. Li and W. Wang, *Chem. Eng. J.*, 2025, **508**, 161080.
26 R. Liu, F. Shi, H. Zhu, K. Liu, Z. Lai, Y. Li, Z. Yang and J. Li, *Anal. Chem.*, 2024, **96**, 15338–15346.
27 W. Gu, Y. Wang, Y. Wu and Q. Huang, *Spectrochim. Acta, Part A*, 2025, **328**, 125459.
28 Z. Yuan, Y. Zhu, L. Xue, D. Ge, S. Xue, Y. Xie, W. Zhang and X. Chen, *Microchem. J.*, 2025, **213**, 113799.
29 B. Hou, X. Guo, Y. Zhang, L. Zhang, D. Zhang, Z. Wu, J. Zhang and Z. Hao, *ACS Sustainable Chem. Eng.*, 2023, **11**, 6211–6219.
30 Y. Zhou, Y. Jiang, Y. Zhang, Y. Chen, Z. Wang, A. Liu, Z. Lv and M. Xie, *ACS Appl. Mater. Interfaces*, 2022, **14**, 32149–32156.
31 A. Zhou, W. Cheng, W. Wang, Q. Zhao, J. Xie, W. Zhang, H. Gao, L. Xue and J. Li, *Adv. Energy Mater.*, 2020, **14**, 2000943.
32 J. Hou, Z. Tang, K. Wei, Q. Lai and Y. Liang, *Catal. Sci. Technol.*, 2021, **11**, 1110–1115.
33 J. Lin, L. Li, E. Fan, C. Liu, X. Zhang, H. Cao, Z. Sun and R. Chen, *ACS Appl. Mater. Interfaces*, 2020, **12**, 18482–18489.
34 N. Kosova, E. Devyatkina and V. Kaichev, *J. Power Sources*, 2007, **174**, 735–740.
35 Y. Lei, X. Lin and H. Liao, *Mater. Chem. Phys.*, 2017, **194**, 128–136.
36 N. Ramgopal, P. Mukherjee, T. Kamilya, N. Basavegowda, M. Mahanthappa, N. Aljarba, R. Alqahtani, S. Alkahtani, J. Park and R. Vishwanath, *Int. J. Biol. Macromol.*, 2025, **288**, 138766.
37 H. Fu, X. Wang, L. Ye, Z. Wu, J. Yang, M. Shi and E. Ang, *Chem. Eng. J.*, 2025, **506**, 160308.
38 Y. Luo, J. Shen, Y. Yao, J. Dai, F. Ling, L. Li, Y. Jiang, X. Wu, X. Rui and Y. Yu, *Adv. Mater.*, 2024, **36**, 2405458.
39 G. Liu, W. Chen, L. Ning, H. Yu, M. Gao, L. Ma, R. Lv, J. Pan and M. Fu, *Desalination*, 2025, **600**, 118489.
40 Y. Zhu, J. Yan, J. Liu, H. Chen, J. Gui, C. Wu, X. Zhu, P. Yin, M. Liu, Y. Zhang and S. Yao, *ACS Appl. Nano Mater.*, 2022, **5**, 15102–15114.
41 C. Gong, B. Chen, Y. Xing and H. Zhao, *J. Hazard. Mater.*, 2024, **463**, 132849.
42 Y. Lin, A. Zhao, Y. Tao, J. Ren and X. Qu, *J. Am. Chem. Soc.*, 2013, **135**, 4207–4210.
43 B. Srinivasan, *FEBS J.*, 2022, **289**, 6086–6098.
44 A. Swaidan, A. Addad, J. Tahon, A. Barras, J. Toufaily, T. Hamieh, S. Szunerits and R. Boukherroub, *Anal. Chim. Acta*, 2020, **1109**, 78–89.
45 M. Ivanova, E. Grayfer, E. Plotnikova, L. Kibis, G. Darabdhara, P. Boruah, M. Das and V. Fedorov, *ACS Appl. Mater. Interfaces*, 2019, **11**, 22102–22112.
46 Y. Wang, T. Li and H. Wei, *Anal. Chem.*, 2023, **95**, 10105–10109.
47 M. Xu, Q. Zhang, Z. Zhu, Y. Xue, T. Zhang and J. Hong, *J. Cleaner Prod.*, 2022, **377**, 134258.
48 X. Xia, X. Zhao, W. Ye and C. Wang, *Electrochim. Acta*, 2014, **142**, 173–181.
49 D. Singhwal and P. Rana, *Mater. Chem. Phys.*, 2024, **314**, 128895.
50 N. Oberleitner, C. Peters, J. Muschiol, M. Kadow, S. Saß, T. Bayer, P. Schaaf, N. Iqbal, F. Rudroff, M. Mihovilovic and U. Bornscheuer, *ChemCatChem*, 2013, **5**, 3524–3528.
51 X. Wang, M. Chen and L. Zhao, *Chem. Eng. J.*, 2023, **468**, 143612.
52 C. Zhou, Y. Zeng, Z. Song, Q. Liu, Y. Zhang, M. Wang and Y. Du, *Anal. Chem.*, 2022, **94**, 13261–13268.
53 L. Zhao, J. Yang, M. Gong, K. Li and J. Gu, *J. Am. Chem. Soc.*, 2021, **143**, 15145–15151.
54 T. Phookum, S. Boobphahom, T. Siripongpreda, S. Ummartyotin and N. Rodthongkum, *Cellulose*, 2024, **31**, 8555–8568.
55 X. Yang, C. Jin, S. Yang and M. Tian, *Sens. Actuators, B*, 2024, **412**, 135849.